Polarized infrared reflectivity of one-dimensional Gaussian sea surfaces with surface reflections

Hongkun Li,* Nicolas Pinel, and Christophe Bourlier

Lunam Université—Université de Nantes—IETR Laboratory, Polytech Nantes, Rue C. Pauc,
La Chantrerie, BP 50609, 44306 Nantes Cedex 3, France

*Corresponding author: hongkun.li@univ-nantes.fr

Sea surface infrared reflectivity is an important parameter in maritime remote sensing. Usually, single reflection by the sea surface is considered. However, a loss of energy is then reported for large zenith observation angles ($\theta > 50°$) with a peak of about 4% for $\theta \approx 80°$, because of the neglect of the multiple surface reflections. This paper presents calculations for the polarized infrared reflectivity of one-dimensional sea surfaces (2D problems) with two surface reflections, by introducing a bistatic illumination function with two reflections. The results show good agreement with the ones obtained by a Monte Carlo ray-tracing method. It is also shown that the energy conservation criterion is better satisfied after considering two surface reflections.   © 2013 Optical Society of America

OCIS codes: (280.5715) Refractivity profiles; (260.3060) Infrared; (000.5490) Probability theory, stochastic processes, and statistics; (290.5880) Scattering, rough surfaces; (010.0280) Remote sensing and sensors.

http://dx.doi.org/10.1364/AO.52.006100

1. Introduction

The knowledge of the sea surface reflectivity ρ is crucial in maritime remote sensing in general, for example, the estimation of sea surface temperature [1], the generation of oceanic images [2–5], the vessel detection [6], etc. The sea surface reflectivity ρ corresponds to the radiance from the sky (atmosphere, sun, etc.) reflected by the sea surface. It depends on the incidence and observation directions. However, it is also commonly averaged on the incidence or the observation direction over the upper hemisphere to obtain a hemispherical average reflectivity.

Published models of infrared reflectivity usually take into account one surface reflection [3,7–9], as illustrated in Fig. 1. In these models, shadowing due to the surface roughness is taken into account with single surface reflection.

The law of energy conservation implies that the sum of the absorbed and reflected energy equals the incident one. However, Yoshimori *et al.* [9] proved that a loss of energy of up to 4% is found for large zenith observation angles (corresponding to a receiver close to the horizon) if multiple surface reflections were ignored.

Multiple surface reflections are seldom studied because of their complexity. To take into account multiple reflections by the rough surfaces, the key lies in the determination of the probability that multiple surface reflections occur, which is expressed by a bistatic illumination function with n surface reflections. Lynch and Wagner [10] built a bistatic illumination function with two surface reflections (see Fig. 2), with which they calculated the scattered energy by a rough surface which was assumed to be a perfect reflector. They pointed out that the energy conservation criterion was better satisfied after considering the second reflection. Bourlier *et al.* [11] developed a bistatic illumination function with multiple surface reflections as the product of
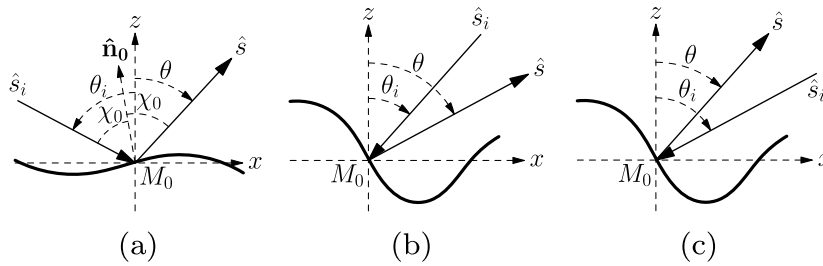
Fig. 1. Three cases of single surface reflection for 1D surfaces. (a) In case 1, the transmitter and the receiver are on different sides ($\theta \geq 0$, $\theta_i < 0$), while in (b) case 2 and (c) case 3, they are on the same side ($\theta \geq 0$, $\theta_i > 0$), with the receiver being lower ($\theta \geq \theta_i$) in (b) and higher ($\theta < \theta_i$) in (c).

successive monostatic illumination functions. However, this model has not been compared with any numerical results or with measurements. In the model of Schott *et al.* [12], a Monte Carlo ray-tracing method was developed to calculate the infrared reflectivity of a rough dielectric surface with multiple reflections. They arrived at the same conclusion that the energy conservation criterion was better satisfied when the second surface reflection was considered.

This paper develops an analytical model to determine the sea surface reflectivity in the infrared atmospheric transmission windows ($\lambda \in [3, 5]$ and $[8, 12]$ μm). Polarization is studied, which may provide additional information in measuring and analyzing signals [13]. Two surface reflections are considered by introducing an improved bistatic illumination function with two surface reflections. A Monte Carlo ray-tracing method is used as a reference method. To further evaluate the performance of the model, the energy conservation criterion is examined.

In this paper, one-dimensional Gaussian sea surfaces (1D surfaces, 2D problems) of infinite length are considered, which are defined by the profiles of 2D surfaces along a given wind direction. The surfaces are modeled as single-valued, thus whitecaps and breaking waves are not taken into account. The geometric optics (GO) approximation is assumed to be valid as the infrared wavelengths studied here (≈ 10 μm) are much smaller than the radius of curvature of the capillary waves (several millimeter) of sea surfaces [14]. Under such an approximation, only specular reflections are considered. This model can be applied to other bands where GO is valid.
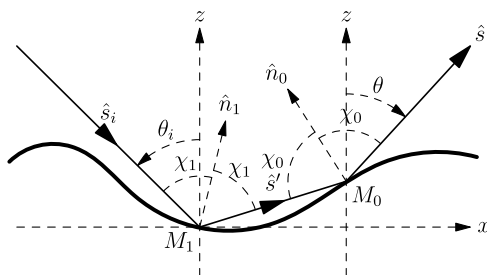
This paper is organized as follows. In Section 2, the bistatic illumination function with one surface reflection is briefly recalled, then it is extended to take into account two surface reflections. In Section 3, the polarized infrared reflectivity of sea surfaces with one and that two reflections are derived. In Section 4, the numerical results of the bistatic illumination functions and of the sea surface reflectivity are shown and compared with those obtained by a Monte Carlo ray-tracing method. Then the energy conservation criterion is examined.

2. Bistatic Illumination Function

When solving rough or sea surface infrared reflectivity ρ, shadowing from the transmitter and the receiver must be taken into account, especially for grazing incidence and/or observation directions. On the other hand, the incidence ray may undergo multiple surface reflections before it is reflected into the observation direction.

To take into account these phenomena, a bistatic illumination function S_B^n is employed, where $n = 1, 2, 3, \ldots$ denotes the number of reflections and the subscript "B" stands for the bistatic configuration. In this section, the widely used S_B^1 with one reflection is recalled, and a model S_B^2 with two reflections is derived. We recall that the surfaces are assumed to be single valued and only specular reflections are considered.

A. S_B^1 with One Reflection

To evaluate the shadowing effect in the incidence and the observation directions, a bistatic illumination function with one surface reflection S_B^1 is used, which gives the probability that the incidence ray is reflected once by the surface to the receiver. This paper follows the idea of Wagner [15] to extend the monostatic illumination function of Smith [16] to a bistatic configuration.

Three examples of single surface reflection on an arbitrary surface point M_0 with height ζ_0 and slope γ_0 are illustrated in Fig. 1. A system of coordinates (x, z) is defined, with x being the horizontal direction toward the receiver and z being the direction of the zenith. Angles are oriented, with the clockwise direction (that of θ) being the positive direction.

Fig. 2. Incidence ray $\hat{s}_i$ is reflected twice by the surface into the observation direction $\hat{s}$.

1. Statistical Expression of $S_B^1(\theta, \theta_i, \gamma_0, \zeta_0)$

The inverse path is used here, which means that the ray is emitted by the receiver along $\hat{s}^-$ and is reflected by the point M_0 to the transmitter along $\hat{s}_i^-$. The superscript "–" means the inverse of direction. Mathematically, the bistatic illumination function with one surface reflection S_B^1 can be expressed as [15,17,18]

$$S_B^1(\theta, \theta_i, \gamma_0, \zeta_0) = p(abc) = p(ac)p(b|ac), \quad (1)$$

where the definitions of the symbols are given below:

- "the ray $M_0(\hat{s})$ does not intersect the surface" is defined as a;
- "the reflection ray of $M_0(\hat{s})$ propagates in the $\hat{s}_i^-$ direction" is defined as b;
- "the ray $M_0(\hat{s}_i^-)$ does not intersect the surface" is defined as c.

The conditional probability $p(b|ac)$ can be expressed by a Dirac delta function

$$p(b|ac) = \delta(\theta_i^{\mathrm{spe}} - \theta_i), \quad (2)$$

where θ_i^{spe} is the zenith angle of the specular reflection ray of $\hat{s}^-$ (inverse path). The probabilities $p(a)$ and $p(c)$ can both be expressed by the Smith monostatic illumination function S_M (see [16] and [19] for details). The key lies in studying the dependence between the events a and c.

In case 1 shown in Fig. 1(a), where the transmitter and the receiver are on different sides of M_0 with respect to the zenith direction ($\theta \geq 0$, $\theta_i < 0$), it is assumed that a and c are independent. As a result, $p(ac)$ is expressed as [15,17,18]

$$
\begin{aligned}
p(ac) &\approx p(a)p(c) \\
&= S_M(\theta, \gamma_0, \zeta_0) S_M(\theta_i, \gamma_0, \zeta_0) \\
&= F(\zeta_0)^{\Lambda(\mu) + \Lambda^-(\mu_i)}, \quad (3)
\end{aligned}
$$

where F is the cumulative density function, and $\mu_i = \cot \theta_i$, $\mu = \cot \theta$ are the slopes of the incidence and the observation directions, respectively. Λ and Λ^- correspond to rays propagating toward and away from the positive direction of x, respectively (see [19]). Equation (3) does not consider the correlation between the heights and the slopes of different surface points. See [19] for the calculation of the correlation.

In case 2 shown in Fig. 1(b), where the transmitter and the receiver are on the same side of M_0 ($\theta \geq 0$, $\theta_i \geq 0$) with the receiver being lower ($\theta \geq \theta_i$), for single-valued surfaces, it is sure that $M_0(\hat{s}_i^-)$ will not intersect the surface given that $M_0(\hat{s})$ does not ($p(c|a) = 1$). In this case, $p(ac)$ is expressed as [15,17,18]

$$p(ac) = p(a)p(c|a) \approx p(a) = F(\zeta_0)^{\Lambda(\mu)}. \quad (4)$$

Similarly, in case 3 shown in Fig. 1(c), where the locations of the transmitter and the receiver are inverted ($\theta \geq 0$, $\theta_i > 0$, $\theta_i > \theta$) compared to case 2, $p(ac)$ is expressed as [15,17,18]

$$p(ac) = p(c)p(a|c) \approx p(c) = F(\zeta_0)^{\Lambda(\mu_i)}. \quad (5)$$

2. Bidirectional Average $\bar{S}_B^1(\theta, \theta_i)$

The bidirectional average bistatic illumination function $\bar{S}_B^1$ corresponds to the probability that the incidence ray $\hat{s}^-$ leaves the surface along the $\hat{s}_i^-$ direction after it is reflected once by the surface. It is obtained by averaging S_B^1 over the heights and the slopes of the surface, given by

$$\bar{S}_B^1(\theta, \theta_i) = \langle S_B^1(\theta, \theta_i, \gamma_0, \zeta_0) \rangle_1, \quad (6)$$

where $\langle \cdots \rangle_1$ corresponds to the statistical average given by

$$\langle \cdots \rangle_1 = \int_{-\infty}^{+\infty} \int_{-\infty}^{+\infty} \cdots p(\zeta_0, \gamma_0) \mathrm{d}\zeta_0 \mathrm{d}\gamma_0 \quad (7)$$

with $p(\zeta_0, \gamma_0)$ being the joint probability density function (PDF) of the heights and slopes of the surface point M_0.

To evaluate the performance of the model, a Monte Carlo ray-tracing method is used. However, it is nearly impossible to observe a reflection angle θ_i^{spe} (inverse path) of the same value as the given θ_i when a Monte Carlo ray-tracing method is used. As a result, the Dirac delta function $\delta(\theta^{\mathrm{spe}} - \theta_i)$ is replaced by a unitary rectangular window function, with a half-width $\Delta\theta_i$, given by

$$W(\theta_i, \theta_i^{\mathrm{spe}}, \Delta\theta_i) = \begin{cases} 1, & \text{for } |\theta_i^{\mathrm{spe}} - \theta_i| \leq \Delta\theta_i \\ 0, & \text{otherwise} \end{cases}. \quad (8)$$

Then, the integration over the slopes γ_0 of M_0 on the Dirac delta function is replaced by that on a window corresponding to $\theta_i^{\mathrm{spe}} \in [\theta_i - \Delta\theta_i, \theta_i + \Delta\theta_i]$, which gives the probability that the reflection ray $\hat{s}_i^-$ forms an angle θ_i^{spe} in this region with the zenith. In this paper, $\Delta\theta_i = 0.1°$ is used.

Accordingly, in the ray-tracing method, it is assumed that rays with $\theta_i^{\mathrm{spe}} \in [\theta_i - \Delta\theta_i, \theta_i + \Delta\theta_i]$ (inverse path) all reach the transmitter. By doing so, the results of the analytical model and those of the numerical ray-tracing model can be compared directly without difficulty.

3. Hemispherical Average $\bar{S}_B^1$, hemi(θ)

The hemispherical average bistatic illumination function $\bar{S}_B^{1,\mathrm{hemi}}$ corresponds to the probability that the incidence ray $\hat{s}^-$ leaves the surface in any direction after it is reflected once by the surface. It is obtained by averaging S_B^1 over the heights and the slopes of M_0, and over θ_i on the upper hemisphere $\theta_i \in [-\pi/2, \pi/2]$, given by

$$\bar{S}_B^{1,\text{hemi}}(\theta) = \left\langle \int_{-\pi/2}^{\pi/2} S_B^1(\theta, \theta_i, \gamma_0, \zeta_0) \mathrm{d}\theta_i \right\rangle_1, \qquad (9)$$

where $\langle \cdots \rangle_1$ is given by Eq. (7).

B. S_B^2 with Two Reflections

The incidence ray may undergo multiple reflections before it reaches the receiver. This section considers two reflections. Figure 2 illustrates the geometry of this problem for 1D surfaces. An incidence ray $\hat{s}_i$ intersects the surface at M_1, where it is reflected into a direction $\hat{s}'$. Then, the ray $\hat{s}'$ intersects the surface again, where it is reflected to the observation direction $\hat{s}$.

1. Statistical Expression of $S_B^2(\theta, \theta_i, \gamma_0, \zeta_\theta, \gamma_1, \zeta_1)$

To evaluate the probability of observing double surface reflections, a bistatic statistical illumination function with two surface reflections S_B^2 is developed from the monostatic statistical illumination function without reflection S_M^0 by Smith [16] and from that with one reflection S_M^1 by Li et al. [19].

In the calculation, the inverse path is used here. To express the bistatic illumination function with two reflections S_B^2, 4 events are defined:

• "the ray $M_0(\hat{s})$ does not intersect the surface" is denoted as a;
• "the reflection ray $M_0(\hat{s}'^-)$ of $M_0(\hat{s}^-)$ intersects the surface" is denoted as b;
• "the reflection ray of $M_0(\hat{s}'^-)$ propagates in the $\hat{s}_i^-$ direction" is denoted as c;
• "the ray $M_1(\hat{s}_i^-)$ does not intersect the surface" is denoted as d.

The bistatic illumination function S_B^2 is then given by

$$S_B^2(\theta, \theta_i, \gamma_0, \zeta_0, \gamma_1, \zeta_1) = p(abcd)$$
$$= p(ab)p(c|ab)p(d|abc). \quad (10)$$

Determination of $p(ab)$. It is notable that the first part $p(ab)$ equals the monostatic illumination function with one surface reflection S_M^1. This paper uses the model of Li et al. [19]. The probability $p(ab)$ is developed according to four cases, shown in Fig. 3 [19]. The reader is referred to [19] for details about the calculation.

The inverse path is used, which means that a ray $\hat{s}^-$ is reflected by M_0 to M_1, with θ_{01} being the global reflection angle. In cases 1 and 2, the ray $M_0(\hat{s}'^-)$ propagates rightward ($\theta_{01} > 0$), whereas in cases 3 and 4, it propagates leftward ($\theta_{01} < 0$). In cases 1 and 4, it propagates downward ($|\theta_{01}| > 90°$), whereas in cases 2 and 3, it propagates upward ($|\theta_{01}| < 90°$). For uncorrelated surfaces, the monostatic illumination function with one surface reflection is defined according to these 4 cases, given by [19]

$$p(ab) = \Upsilon(\mu - \gamma_0)F(\zeta_0)^{\Lambda(\mu)}$$
$$\times \begin{cases} 1 & \text{for cases 1 and 4,} \\ 1 - F(\zeta_0)^{\Lambda^-(\mu')} & \text{for cases 2 and 3,} \end{cases} \quad (11)$$

where $\Upsilon(\mu - \gamma_0)$ is the unit step function. Note that when $0 < \theta_{01} < \theta$, $p(ab) = p(a)p(b|a)$ equals 0, as given "$M(\hat{s})$ does not intersect the surface," it is impossible that "$M(\hat{s}'^-)$ intersects the surface" (see Fig. 3 of [19] for discussion). As a result, in case 2, only the region $\theta < \theta_{01} < 90°$ is considered. The reader is referred to [19] for the result for correlated surfaces.

Determination of $p(c|ab)$. The second part $p(c|ab)$ corresponds to the probability that the reflection ray of $\hat{s}'^-$ propagates along the $\hat{s}_i^-$ direction. As discussed in S_B^1, it is expressed by a Dirac delta function, given by

$$p(c|ab) = \delta(\theta_i^{\text{spe}} - \theta_i), \qquad (12)$$

where θ_i^{spe} is the zenith angle of the specular reflection ray of $\hat{s}'^-$.

Determination of $p(d|abc)$. The conditional probability $p(d|abc)$ is the conditional probability that M_1 is viewed by the transmitter along the $\hat{s}_i^-$ direction, given "a", "b," and "c." It can be expressed by the monostatic illumination function S_M, except for the cases where obvious correlations are found between the event "d" and "abc," which are discussed below.

In case 1 shown in Fig. 3(a) for the region $-90° < \theta_i < \theta_{10}$, and in case 4 shown in Fig. 3(d) for the region $\theta_{10} < \theta_i < 90°$ (denoted with red double arc), it is impossible that "the ray $M_1(\hat{s}_i^-)$ does not intersect the surface" (event d) given that "$M_0(\hat{s}'^-)$
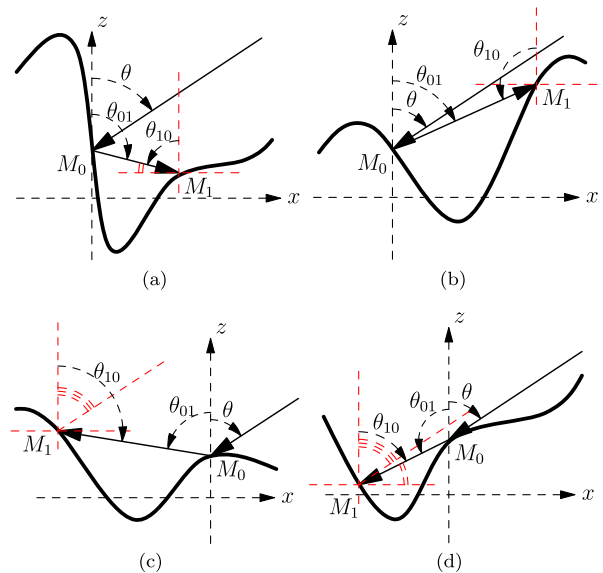

Fig. 3. Four configurations of surface reflections (inverse path), with the reflection ray $M_0(\theta_{01})$ propagating. (a) Case 1, rightward and downward. (b) Case 2, rightward and upward. (c) Case 3, leftward and upward. (d) Case 4, leftward and downward.

intersects the surface at M_1" (event b), which means that $p(d|abc) = 0$. In cases 3 and 4 shown in Figs. 3(c) and 3(d) for the region $0° < \theta_i < \theta$ (denoted with red triple arc), it is sure that the ray $M_1(\hat{s}_i^-)$ does not intersect the surface (event d) given "$M_0(\hat{s})$ does not intersect the surface" (event a), which means that $p(d|abc) = 1$. Besides these situations, $p(d|abc)$ is expressed by the monostatic illumination function S_M. To sum up, the conditional probability $p(d|abc)$ is given by

$$p(d|abc) = \begin{cases} \begin{bmatrix} 0, & -90° < \theta_i < \theta_{10}, \\ p(d), & \text{other } \theta_i, \end{bmatrix} & \text{case 1,} \\ \quad p(d), & \text{case 2,} \\ \begin{bmatrix} 1, & 0° < \theta_i < \theta, \\ p(d), & \text{other } \theta_i, \end{bmatrix} & \text{case 3,} \\ \begin{bmatrix} 1, & 0° < \theta_i < \theta, \\ 0, & \theta_{10} < \theta_i < 90°, \\ p(d), & \text{other } \theta_i, \end{bmatrix} & \text{case 4,} \end{cases}$$

(13)

where for uncorrelated surfaces $p(d)$ is given by

$$p(d) = \begin{cases} F(\zeta_1)^{\Lambda(\mu_i)}, & \text{for } \theta_i > 0, \\ F(\zeta_1)^{\Lambda^-(\mu_i)}, & \text{for } \theta_i > 0. \end{cases}$$

(14)

The bistatic illumination function with two reflections S_B^2 is then obtained by substituting Eqs. (11)–(13) for Eq. (10).

It is notable that the bistatic illumination function defined here is mathematically the same as the model of Lynch and Wagner [10] for uncorrelated surfaces with even surface slope PDFs. As a result, the uncorrelated model with Gaussian slope PDF developed here gives the same result as that of Lynch and Wagner. The advantage of the model presented here is the permission to take into account the correlation between surface points to improve the performance.

2. Bidirectional Average $\bar{S}_B^2(\theta, \theta_i)$

The bidirectional average bistatic illumination function $\bar{S}_B^2$ corresponds to the probability that the incidence ray $\hat{s}^-$ leaves the surface along the $\hat{s}_i^-$ direction after it is reflected twice by the surface. It is obtained by averaging S_B^2 over the heights and the slopes of the surface points M_1 and M_0, given by

$$\bar{S}_B^2(\theta, \theta_i) = \langle S_B^2(\theta, \theta_i, \gamma_0, \zeta_0, \gamma_1, \zeta_1)\rangle_2, \quad (15)$$

where $\langle\cdots\rangle_2$ is given by

$$\langle\cdots\rangle_2 = \int_{-\infty}^{+\infty}\int_{-\infty}^{+\infty}\int_{-\infty}^{+\infty}\int_{-\infty}^{+\infty}\cdots p(\gamma_0,\zeta_0,\gamma_1,\zeta_1)\mathrm{d}\zeta_1\mathrm{d}\gamma_1\mathrm{d}\zeta_0\mathrm{d}\gamma_0$$

(16)

with $p(\gamma_0, \zeta_0, \gamma_1, \zeta_1)$ being the joint PDF of the heights and slopes of surface points M_0 and M_1.

For the same reason stated at the end of Section 2.A, the Dirac delta function used in $p(c|ab)$ is replaced by a unitary window function given by Eq. (8).

3. Hemispherical Average $\bar{S}_B^2$, hemi(θ)

The hemispherical average bistatic illumination function $\bar{S}_B^{2,\mathrm{hemi}}$ corresponds to the probability that the incidence ray $\hat{s}^-$ leaves the surface after it is reflected twice. It is obtained by averaging S_B^2 over the heights and the slopes of the surface points M_1 and M_0, and over θ_i on the upper hemisphere $\theta_i \in [-\pi/2, \pi/2]$, given by

$$\bar{S}_B^{2,\mathrm{hemi}}(\theta) = \left\langle \int_{-\pi/2}^{\pi/2} S_B^2(\theta, \theta_i, \gamma_0, \zeta_0, \gamma_1, \zeta_1)\mathrm{d}\theta_i \right\rangle_2, \quad (17)$$

where $\langle\cdots\rangle_2$ is given by Eq. (16).

Note that when calculating the integration in $\langle\cdots\rangle_2$, the slope PDF of the surface point M_1 is different from that of the surface, given that M_1 is the intersection point of the ray $\hat{s}'^-$ and the rough surface. Following the discussion in [19], the slope PDF of M_1 is given by

$$p_{\gamma_1}(\gamma_1) = \begin{cases} \dfrac{\Upsilon(\gamma_1-\mu_1)}{\int_{\mu_1}^{+\infty} p_\gamma(t)\mathrm{d}t}p_\gamma(\gamma_1), & \text{for cases 1 and 2,} \\ \dfrac{\Upsilon(\mu_1-\gamma_1)}{\int_{-\infty}^{\mu_1} p_\gamma(t)\mathrm{d}t}p_\gamma(\gamma_1), & \text{for cases 3 and 4,} \end{cases}$$

(18)

where p_γ is the marginal surface slope PDF.

The bidirectional and hemispherical average bistatic illumination functions are used to calculate the bidirectional and hemispherical reflectivity of the sea surface in Section 3, respectively.

3. Infrared Reflectivity and Energy Conservation

In this section, the sea surface infrared reflectivity ρ is calculated. The infrared reflectivity with one reflection ρ_1 is derived in Section 3.A, and the one with two reflections ρ_2 is derived in Section 3.B.

A. Reflectivity with One Reflection

The sea surface infrared reflectivity with one surface reflection corresponds to the radiance from the sky reflected once by the surface into the observation direction, as illustrated in Fig. 1.

For 1D surfaces, the local angle of incidence χ_0 of an arbitrary surface point M_0 is given by [see Fig. 1(a)]

$$\cos \chi_0 = \hat{n}_0 \cdot \hat{s} = \frac{\cos \theta - \gamma_0 \sin \theta}{\sqrt{1 + \gamma_0^2}}, \quad (19)$$

where $\hat{n}_0$ is the unitary vector normal to M_0 and γ_0 is its slope. The local reflectivity of M_0 is then given by

$$\rho_{1,H,V}^{\text{local}}(\chi_0) = |r_{H,V}(\chi_0)|^2, \tag{20}$$

where $r_{H,V}$ is the Fresnel reflection coefficients in horizontal or vertical polarization, respectively, given by

$$r_H(\chi) = \frac{\cos\chi - n\cos\chi'}{\cos\chi + n\cos\chi'}, \quad r_V(\chi) = \frac{n\cos\chi - \cos\chi'}{n\cos\chi + \cos\chi'}, \tag{21}$$

where n is the index of refraction of the sea water, and χ' is the local angle of refraction given by Snell's law

$$\sin(\chi') = \frac{\sin(\chi)}{n}. \tag{22}$$

It is notable that, for 1D surfaces, the incidence direction $\hat{s}_i$, the observation direction $\hat{s}$ and the local normal $\hat{n}_0$ to any arbitrary surface point belong to the same plane [the (x, z) plane here]. As a result, the horizontal polarization directions H and H_i corresponding to $\hat{s}$ and $\hat{s}_i$, respectively, are then identical, as they are both perpendicular to the (x, z) plane. In addition, H and H_i do not change from point to point [14]. As a result, cross-polarization does not occur for 1D surfaces.

The bidirectional sea surface infrared reflectivity with one surface reflection is the average of the local reflectivity over the surface, given by [7]:

$$\rho_{1,H,V}(\theta, \theta_i) = \langle |r_{H,V}(\chi_0)|^2 g_0 S_B^1 \rangle_1, \tag{23}$$

where $\langle \cdots \rangle_1$ is given by Eq. (7). The term g_0 results from projecting the area of the facet around M_0 onto the orthogonal direction of the observation direction $\hat{s}$, given by

$$g_0 = 1 - \gamma_0 \tan\theta. \tag{24}$$

S_B^1 is the bistatic illumination function with one reflection given by Eqs. (3)–(5).

The hemispherical sea surface infrared reflectivity with one reflection is obtained by integrating the bidirectional one over θ_i on the upper hemisphere $\theta_i \in [-\pi/2, \pi/2]$, given by

$$\rho_{1,H,V}^{\text{hemi}}(\theta) = \left\langle \int_{-\pi/2}^{+\pi/2} |r_{H,V}(\chi_0)|^2 g_0 S_B^1 d\theta_i \right\rangle_1. \tag{25}$$

B. Reflectivity with Two Reflections

The sea surface infrared reflectivity with two surface reflections corresponds to the radiance from the sky reflected twice by the surface into the observation direction, as illustrated in Fig. 2.

As the incidence ray is reflected twice by the surface, the local polarized reflectivity with two surface reflections is then given by

$$\rho_{2,H}^{\text{local}} = |r_{H_1}(\chi_1)|^2 |r_H(\chi_0)|^2,$$
$$\rho_{2,V}^{\text{local}} = |r_{V_1}(\chi_1)|^2 |r_V(\chi_0)|^2, \tag{26}$$

where the directions of polarizations H_1 and V_1 are defined by the local normal $\hat{n}_1$ of M_1 and the direction of propagation $\hat{s}'$. The local angle of incidence χ_1 at M_1 is calculated by Eq. (19), by replacing γ_0 and θ with γ_1 and θ_i, respectively. As we stated before, cross polarization does not occur for 1D surfaces.

The bidirectional reflectivity $\rho_{2,H,V}$ of sea surfaces with two surface reflections is the average of the local reflectivity over the whole surface, given by

$$\rho_{2,H,V}(\theta, \theta_i) = \langle \rho_{2,H,V}^{\text{local}} g_0 S_B^2 \rangle_2, \tag{27}$$

where $\langle \cdots \rangle_2$ is given by Eq. (16) and S_B^2 is the bistatic illumination function with two surface reflections given by Eq. (10).

The hemispherical sea surface infrared reflectivity with two reflections is obtained by integrating the bidirectional one over θ_i on the upper hemisphere $\theta_i \in [-\pi/2, \pi/2]$, given by

$$\rho_{2,H,V}^{\text{hemi}}(\theta) = \left\langle \int_{-\pi/2}^{+\pi/2} \rho_{2,H,V}^{\text{local}} g_0 S_B^2 d\theta_i \right\rangle_1. \tag{28}$$

C. Energy Conservation

Following the law of energy conservation, under thermal equilibrium, the sum of the absorbed and reflected energy equals the incident energy. In other words, the sum of the surface emissivity and hemispherical average reflectivity equals 1

$$\varepsilon(\theta) + \rho^{\text{hemi}}(\theta) = 1. \tag{29}$$

It is reported that this condition is not fulfilled if only the direct emissivity ε_0 and the hemispherical reflectivity with one reflection ρ_1^{hemi} are considered, with $\varepsilon_0 + \rho_1^{\text{hemi}} < 1$ for large θ [9]. Yoshimori *et al.* [9] stated that it was because multiple surface reflections were neglected.

In this paper, the law of energy conservation is examined, by taking into account the emissivity ε_1 with one reflection [14,20–23] and the hemispherical reflectivity with two reflections ρ_2^{hemi}. In this paper, the emissivity model ε_1 of Li *et al.* [14] is used.

4. Numerical Results

In this section, the numerical results of the bistatic illumination function and the surface infrared reflectivity are analyzed. Recall that 1D surfaces are considered. The models are compared with a Monte Carlo ray-tracing method. The reader is referred to Appendix A for details about this method.

When calculating the correlated bistatic illumination function, it is assumed that the joint PDF of the surface heights and slopes is Gaussian, and the height autocorrelation function is also Gaussian (see [7] for the calculation of the correlation). In other

cases, it is assumed that the surface slopes and heights of surface points are uncorrelated. For uncorrelated surfaces, the knowledge of the surface height PDF is not necessary. The surface slope PDF is assumed to be Gaussian with zero mean, given by

$$p_\gamma(\gamma) = \frac{1}{\sqrt{2\pi}\sigma_\gamma} \exp\left(-\frac{\gamma^2}{2\sigma_\gamma^2}\right), \tag{30}$$

where σ_γ is the RMS slope of the sea surface. In this paper, the result of Cox and Munk is used, which relates the surface RMS slope to the wind speed u_{12} at 12.5 m above the sea surface [24]. The upwind direction is considered here, for which the RMS slope is given by

$$\sigma_\gamma^2 = 3.16 \times 10^{-3} u_{12}. \tag{31}$$

The reflectivity in the infrared atmospheric transmission windows is calculated. The index of refraction of the sea water n is given by the model of Hale and Querry [25]. For example, for wavelengths $\lambda = \{4; 10\}$ μm, the index of refraction $n = \{0.3510 + 0.0046i; 1.2180 + 0.0508i\}$.

As stated in Section 2.A, the Dirac delta functions in S_B^1 and S_B^2 are replaced by the window function given by Eq. (8) during the calculation for a direct comparison with the Monte Carlo ray-tracing method. The integrations in the bistatic illumination functions $\bar{S}_B^1, \bar{S}_B^{1,\mathrm{hemi}}, \bar{S}_B^2, \bar{S}_B^{2,\mathrm{hemi}}$ and in the reflectivity $\rho_1, \rho_1^{\mathrm{hemi}}, \rho_2, \rho_2^{\mathrm{hemi}}$ are calculated numerically, as they do not have analytical solutions.

A. Illumination Function with One Reflection

For given directions θ and θ_i, the average bistatic illumination function with one reflection $\bar{S}_B^1$ is given by Eq. (6). The results are shown in Fig. 4. The wind speed at 12.5 m above the sea surface is $u_{12} = 10$ m/s (sea surfaces with Beaufort scale ≈5). $\bar{S}_B^1$ is plotted versus θ_i, for three values of $\theta = \{30°, 60°, 80°\}$. The results for $u_{12} = 5$ m/s are also calculated (as well as in all other simulations in this paper), which are not shown as they leads to the same conclusion.

It is shown that the uncorrelated and the correlated models both agree very well with the Monte Carlo ray-tracing model. For the three observation directions $\theta = \{30°, 60°, 80°\}$, the average bistatic illumination function $\bar{S}_B^1$ has a maximum around the global specular reflection direction $\theta = \{-30°, -60°, -80°\}$, respectively, meaning that it is most likely to observe a reflection ray around the global specular reflection direction of the incidence ray.

The hemispherical average bistatic illumination function with one surface reflection $\bar{S}_B^{1,\mathrm{hemi}}$ is obtained by Eq. (9). The results are shown in Fig. 5 for a wind speed $u_{12} = 10$ m/s.

It is shown that the hemispherical average bistatic illumination function $\bar{S}_B^{1,\mathrm{hemi}}$ decreases monotonously with the observation angle θ. For surfaces with wind
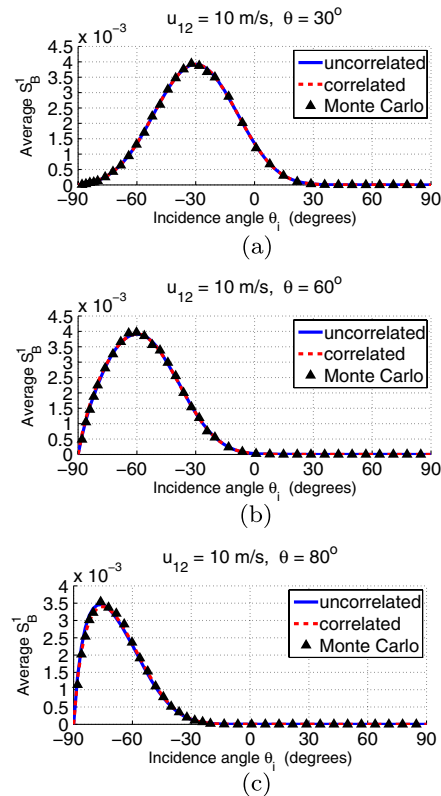

Fig. 4. Average bistatic illumination function with one reflection $\bar{S}_B^1$ versus θ_i for three θ: (a) $\theta = 30°$, (b) $\theta = 60°$, and (c) $\theta = 80°$. The wind speed u_{12} is 10 m/s.

speed $u_{12} = 10$ m/s, $\bar{S}_B^{1,\mathrm{hemi}} \approx 1$ for $\theta < 40°$, meaning that shadowing is negligible along both the incidence and reflection directions. Shadowing becomes significant as θ increases. For $\theta \to 90°$, $\bar{S}_B^{1,\mathrm{hemi}} = 0$. This can be predicted by the fact that $S_M(90°) \to 0$ (see Fig. 2 of [16]), meaning that all the surface points are in the shadow of the receiver. The results of the model agree very well with the Monte Carlo ray-tracing results.

B. Illumination Function with Two Reflections

The average bistatic illumination function with two reflections $\bar{S}_B^2$ is given by Eq. (15). The results are
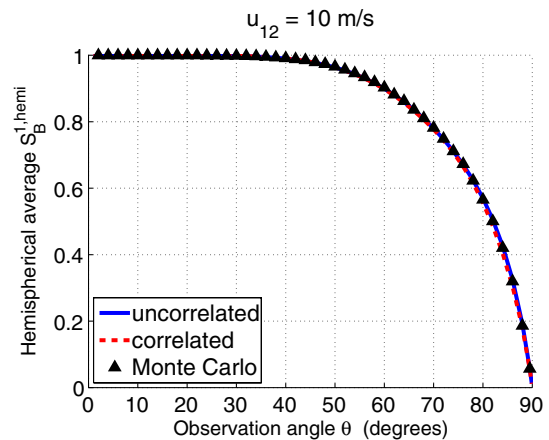

Fig. 5. Hemispherical average bistatic illumination function $\bar{S}_B^{1,\mathrm{hemi}}$ for surfaces with wind speed $u_{12} = 10$ m/s.

shown in Fig. [6] for the same parameters as those in Fig. [4].

Shifts of the maxima between the results of the model and those obtained from the Monte Carlo ray-tracing method are found, especially for the zenith observation angle $\theta = 30°$. The maxima predicted by the model, with or without the correlation between the surface points, occur around $\theta_i \approx -80°$ for different θ, whereas the Monte Carlo ray-tracing results suggest that their locations should significantly depend on the angle θ.

One possible reason for this difference is that the slope PDF of M_1 [Eq. ([18])] is not well calculated. In the derivation of the slope PDF of M_1, it is assumed that any slope γ_1 fulfilling $|\chi_1| < 90°$ can equally be the slope of M_1, which depends only on the slope of $\hat{s}'$, while the influence of the observation angle θ is ignored.

Except for this drawback, the results of the present model are generally of the same level as the ones of the Monte Carlo ray-tracing model. The maxima of $\bar{S}_B^2$ are of the order of 10^{-5}, 10^{-4}, and 10^{-3} (recall that $\Delta\theta_i = 0.1°$) for $\theta = 30°$, $60°$, and $80°$, respectively, which means that double surface reflections are more significant for large zenith observation angles θ.

The hemispherical average illumination function with two surface reflections $\bar{S}_B^{2,\text{hemi}}$ is given by Eq. ([17]). The results are shown in Fig. [7] for a wind speed $u_{12} = 10$ m/s.
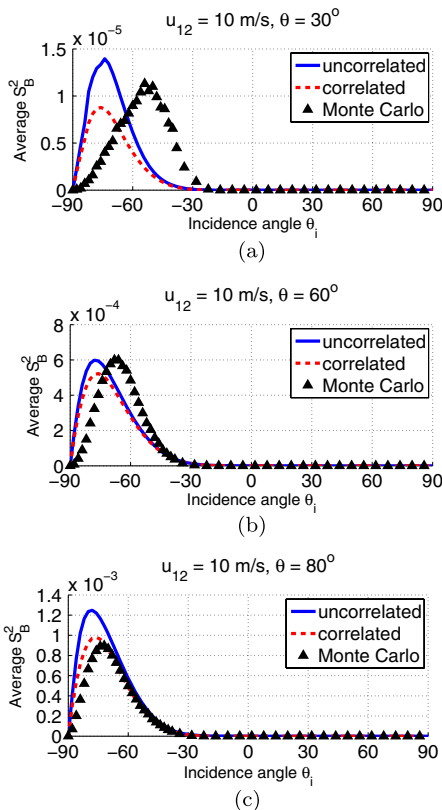

Fig. 6. Average bistatic illumination function with two reflections $\bar{S}_B^2$ versus θ_i, for three θ: (a) $\theta = 30°$, (b) $\theta = 60°$, and (c) $\theta = 80°$. The wind speed u_{12} is 10 m/s.
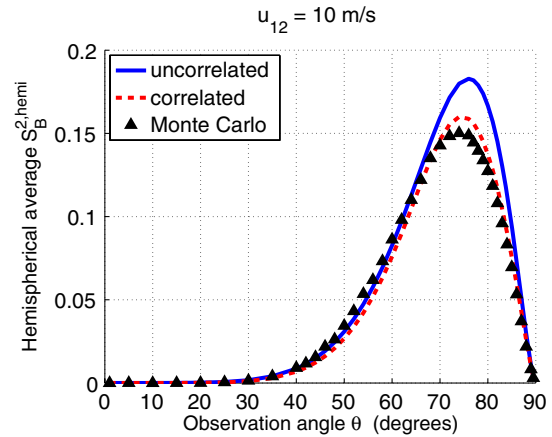

Fig. 7. Hemispherical average bistatic illumination function with two surface reflections for wind speed $u_{12} = 10$ m/s.

It is shown that the model agrees quite well with the Monte Carlo ray-tracing method. The model, correlated or uncorrelated, slightly underestimates the result at small and moderate θ, e.g., $\theta < 65°$, and overestimates the result for large θ. A better agreement is obtained by taking into account the correlation between surface points.

It is notable that double surface reflections are significant only for large zenith observation angles θ. This is predictable, because the bistatic illumination function is based on the monostatic illumination function with one surface reflection [$p(ab)$ in Eq. ([10])], which is significant only in this region (see Fig. 4 of [[14]]).

C. Reflectivity with One Reflection

The bidirectional sea surface infrared reflectivity ρ_1 is given by Eq. ([23]). The results are shown in Fig. [8]. Three observation angles $\theta = \{30°, 60°, 80°\}$ are studied, and the results are shown versus the angle of incidence θ_i. The wavelength is $\lambda = 10$ μm, and the wind speed u_{12} is 10 m/s.

It is shown that the model agrees very well with the Monte Carlo ray-tracing method. Taking into account the correlation between the surface heights and slopes hardly modifies the results.

It is readily visible in Fig. [8] that the H and V polarized reflectivity with one reflection ρ_1 do not equal each other. The V polarized ρ_1 is always smaller, which implies that the reflection ray of an unpolarized ray, whose intensity in any polarization is the same, would be partially polarized, with the intensity in H polarization being stronger.

It is notable that the locations of the peaks of ρ_1 in H and V polarizations are different. In addition, they are not located in the global specular reflection direction. This effect is the most significant for $\theta = 60°$ shown in Fig. [8(b)], where the peaks of ρ_1 in H and V polarizations are shifted to about $\theta_i \approx -70°$ and $\theta_i \approx -85°$, respectively. This effect is reported in the measurements of the sea surface sun glitter [[2],[3]], where the peak of the sun glitter was shifted
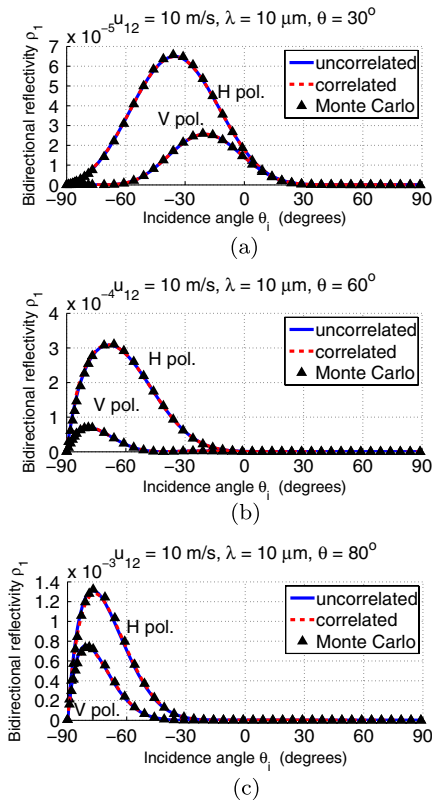
Fig. 8. Bidirectional reflectivity with one reflection ρ_1 versus θ_i, for three θ: (a) $\theta = 30°$, (b) $\theta = 60°$, and (c) $\theta = 80°$. The wind speed u_{12} is 10 m/s and the wavelength is 10 μm.

toward the horizon ($|\theta_i|$ is larger than the one of the global specular reflection direction).

The hemispherical average reflectivity ρ_1^{hemi} is obtained by Eq. (25). The results are shown in Fig. 9 for a wind speed $u_{12} = 10$ m/s and a wavelength $\lambda = 10$ μm.

The model generally agrees well with the Monte Carlo ray-tracing method. For grazing angles $\theta > 80°$, the model slightly overestimates ρ_1^{hemi}. In general, the correlated model gives a better agreement with the Monte Carlo ray-tracing method.
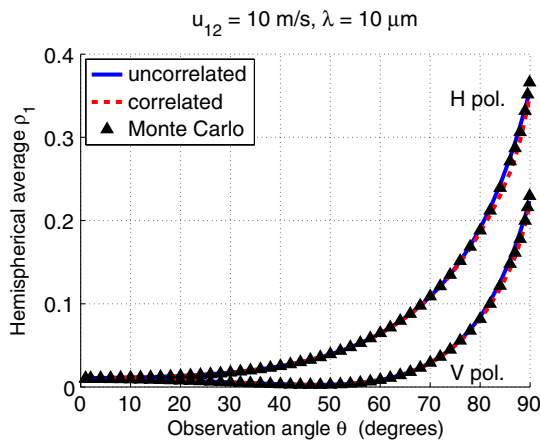

Fig. 9. Hemispherical average infrared reflectivity with one reflection ρ_1^{hemi} versus θ, for $u_{12} = 10$ m/s and $\lambda = 10$ μm.

It is shown that the H polarized ρ_1^{hemi} monotonously increases with the zenith observation angle θ, while the V polarized ρ_1^{hemi} slightly decreases to a minimum and then increases because of the Brewster angle ($\theta_B \approx 50.6°$, for $\lambda = 10$ μm, flat surface). Besides, the H polarized ρ_1^{hemi} is always larger than that in V polarization, which is opposite from the sea surface emissivity ε_0, where $\varepsilon_{0,V}$ is always larger (see Fig. 6 of [14]). This is because, under thermal equilibrium, more waves in one polarization are reflected implies that less waves in this polarization are absorbed (then re-emitted), and vice versa. We may also conclude that V polarized infrared signals better represent the state of sea surfaces (larger $\varepsilon_{0,V}$), whereas H polarized infrared signals better represent the radiance from the sky (larger $\rho_{0,H}$), e.g., the sun glitter.

D. Reflectivity with Two Reflections

The bidirectional sea surface infrared reflectivity ρ_2 is given by Eq. (27). The results are shown in Fig. 10, for the same parameters as those in Fig. 8.

It is shown that for small and moderate zenith observation angles, e.g., $\theta = 30°$ in Figs. 10(a) and 10(b) and 60° in Figs. 10(c) and 10(d), the results of the present model have similar forms to the Monte Carlo ray-tracing results, but the locations of the peaks are different. A better agreement is obtained for large observation angle, $\theta = 80°$ in Figs. 10(e) and 10(f). Note that ρ_2 is much more significant for large θ than for small and moderate ones. Similar discrepancies between the bistatic illumination function S_B^2 and the corresponding Monte Carlo ray-tracing results are found, as shown in Fig. 6. The reason may be that the slope of M_1 is not well calculated.

It is notable that the peaks of ρ_2 do not occur in the global specular reflection directions. As predicted by the Monte Carlo ray-tracing method, double surface reflection shifts the peak of the surface reflectivity from the global specular reflection direction toward the horizon.

The hemispherical average reflectivity with two surface reflections ρ_2^{hemi} is obtained by Eq. (28). The results are shown in Fig. 11 for a wind speed $u_{12} = 10$ m/s and a wavelength $\lambda = 10$ μm.

It is shown that the model agrees quite well with the Monte Carlo ray-tracing result. The uncorrelated model overestimates the surface reflectivity, which is largely overcome after taking into account the correlation between the surface heights and slopes. It is shown that ρ_2^{hemi} is close to zero for small and moderate observation angles θ. It is relatively significant for large observation angles, e.g., $\theta > 70°$.

E. Energy Conservation

The law of energy conservation, given by Eq. (29), is examined here, and the results are shown in Fig. 12, for a wind speed at 12.5 m above the sea surface $u_{12} = 10$ m/s, and for a wavelength $\lambda = 10$ μm.
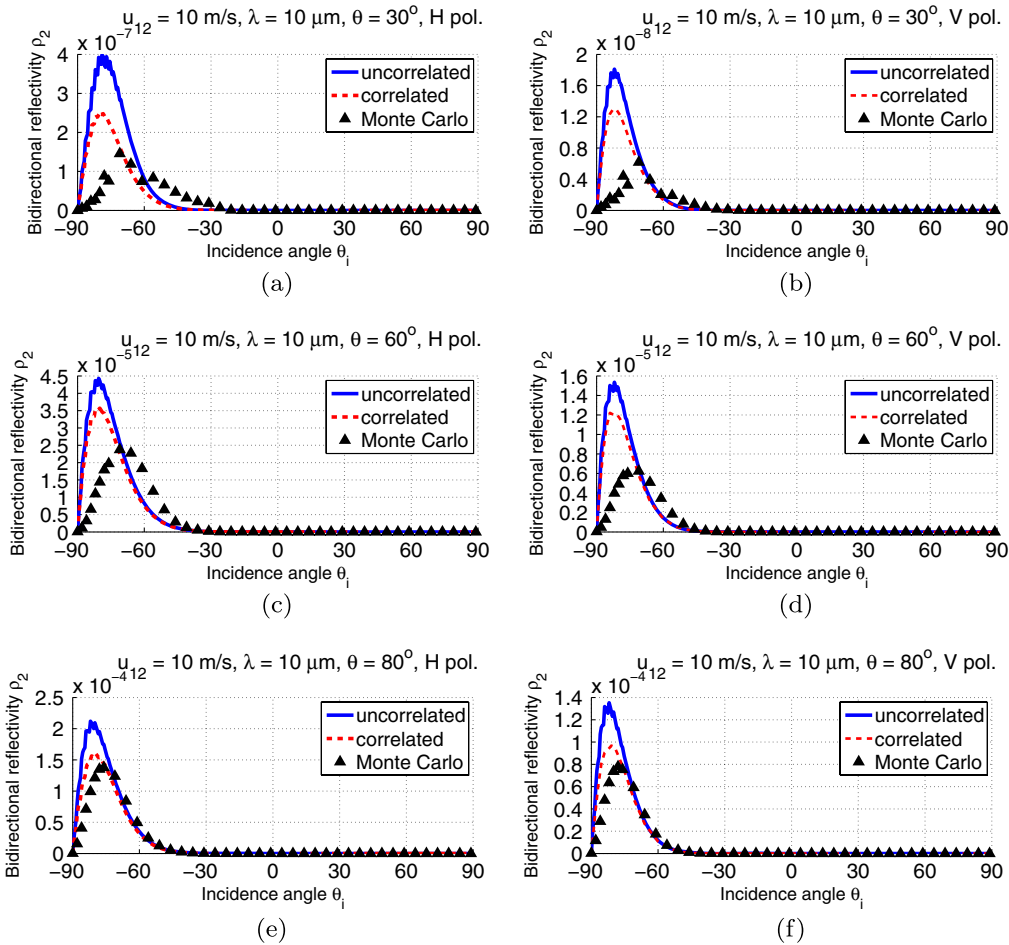
Fig. 10. Bidirectional reflectivity with two reflections ρ_2 versus θ_i, for three values of θ: (first row) $\theta = 30°$, (second row) $\theta = 60°$, and (third row) $\theta = 80°$, in horizontal polarization on the left, and in vertical polarization on the right. The wind speed u_{12} is 10 m/s and the wavelength is 10 μm.

The sea surface emissivity ε_0 and ε_1 are obtained following the model of Li *et al.* [14]. Unpolarized emissivity and reflectivity are considered, which are obtained by averaging the ones in H and V polarizations. The analytical results are compared with those of the Monte Carlo ray-tracing method.
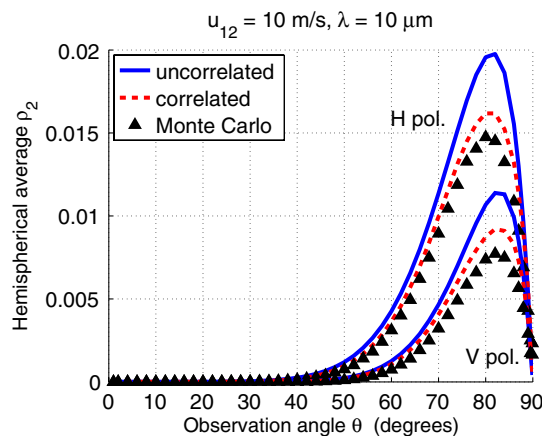

Fig. 11. Hemispherical average infrared reflectivity with two reflection ρ_2^{hemi} with respect to θ for $u_{12} = 10$ m/s and $\lambda = 10$ μm.

When the sea surface infrared emissivity without surface reflection ε_0 and the hemispherical average reflectivity with one reflection ρ_1^{hemi} are considered [Fig. 12(a)], energy is conserved for $\theta < 50°$ ($\varepsilon_0 + \rho_1^{\text{hemi}} \approx 1$). However, $\varepsilon_0 + \rho_1^{\text{hemi}} < 1$ in the region $50° < \theta < 90°$, which means that a loss of energy is predicted. This is because multiple surface reflections are not considered [9]. The minimum is about 0.96 for $\theta \approx 80°$, with a loss of energy being about 0.04 (4% of the incident energy is "lost"). The correlated model shows a sharp peak exceeding 1 for $\theta \approx 88°$, which is due to the poor convergence of the method for grazing θ.

After taking into account the surface infrared emissivity with one reflection ε_1 obtained by the model of Li *et al.* [14] [Fig. 12(b)], the region where energy conservation is checked is extended to $\theta < 60°$. In addition, the peak of the loss of energy is reduced to about 0.02.

Finally, the hemispherical average reflectivity with two reflections ρ_2^{hemi} is taken into account, illustrated in Fig. 12(c). Energy conservation is achieved for almost all θ. Except for the sharp peak of the correlated model, a slight loss of energy is still found for $65° \lesssim \theta \lesssim 85°$, with a peak of about 0.005.
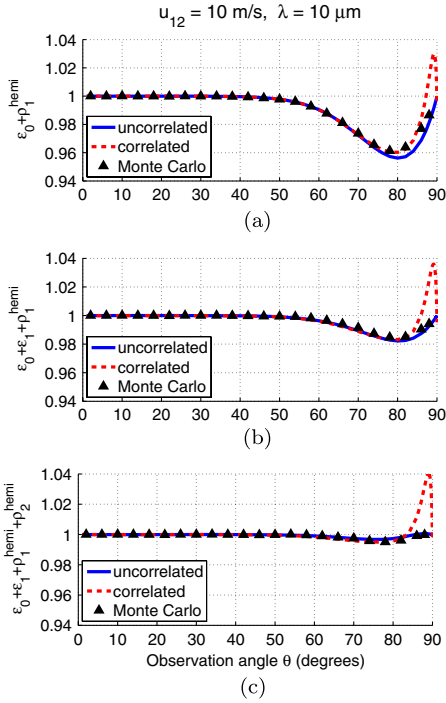
Fig. 12. Verification of the energy conservation. The sum of surface emissivity and hemispherical average reflectivity is shown: (a) $\varepsilon_0 + \rho_1^{\mathrm{hemi}}$ is studied, (b) ε_1 and is taken into account, and (c) then ρ_2^{hemi} is finally considered. The wind speed is $u_{12} = 10$ m/s, and the wavelength is $\lambda = 10$ μm.

The hemispherical average reflectivity $\rho^{\mathrm{hemi}}(\theta)$ is sometimes calculated from $1 - \varepsilon(\theta)$ by using the law of energy conservation [22,26]. Then, the energy conservation criterion is fulfilled by construction. However, energy conservation cannot be achieved for large θ by analytical or numerical methods even after taking into account up to two surface reflections, as shown in Fig. 12. As a result, an overestimation in the reflectivity ρ^{hemi} is predicted for large θ (see also Section 4 of [27] for discussion), especially when multiple surface reflections are ignored in the calculation of the surface emissivity $\varepsilon(\theta)$. Besides, another drawback of this method is that it cannot separate the contribution of each surface reflection in the surface reflectivity.

5. Conclusion

Surface multiple reflections are important when solving rough/sea surface reflectivity for large zenith observation angles. This paper calculates the sea surface infrared reflectivity with two surface reflections by introducing a bistatic illumination function with two surface reflections. A Monte Carlo ray-tracing method is used as reference. It is shown that the model agrees well with the reference, where an overestimation is observed. Taking into account the surface correlation improves the agreement. Then, the law of energy conservation is examined. It is shown that the energy conservation criterion is better satisfied after taking into account the surface infrared emissivity with one reflection ε_1 and the hemispherical average reflectivity with two reflections ρ_2^{hemi}. Cross polarization effect and comparison with measurements are left to further study by considering 2D surfaces.

Appendix A: Monte Carlo Ray-Tracing Method

To evaluate the performance of the model, a Monte Carlo ray-tracing method is used. In this paper, 1D rough surfaces are generated with Gaussian height PDF and Gaussian height autocorrelation function. For a Gaussian autocorrelation function, the correlation length of the surface L_c is given by

$$L_c = \sqrt{2}\sigma_\zeta/\sigma_\gamma, \qquad (A1)$$

where σ_ζ and σ_γ are the RMS height and RMS slope of the surface, respectively. For sea surfaces with a wind speed $u_{12} = 10$ m/s, $\sigma_\zeta \approx 0.46$ m, and $\sigma_\gamma \approx 0.17$ (thus $L_c \approx 3.7$ m), derived from the sea surface spectrum of Elfouhaily *et al.* [28].

The model in this paper is built for surfaces of infinite length. However, it is impossible to perform ray-tracing on a surface of infinite length. Thus, the surface length L is chosen according to the zenith observation angle θ, so that the limited surface length does not cause significant error. In this paper, $L = 200L_c$ for $\theta \leq 70°$, $L = 500L_c$ for $70° < \theta \leq 80°$, and $L = 5000L_c$ for $80° < \theta \leq 90°$ are chosen. The spatial sampling step is 1 cm. The reader is referred to Section 4 of [29] for details about the generation of the surface.

Then, ray-tracing is performed over these surfaces. An incidence ray is sent along $\hat{s}^-$ (inverse path) and all the illuminated surface points (corresponding to M_0) are denoted as a set Ω (see Fig. 4 of [29] for details about the algorithm). The reflection rays are traced. The surface points for which the reflection rays do not intersect the surface again correspond to single surface reflection, noted as a set Ω_1. The other points in Ω correspond to two and more surface reflections, noted as Ω_{2+}. The reflection rays in Ω_{2+}, corresponding to $\hat{s}'^-$ in Fig. 2, intersect the surface in M_1 and are reflected again. The reflection rays ($\hat{s}_i^-$ in Fig. 2) are traced, and the ones which do not intersect the surface again is noted as Ω_2. The other points in Ω_{2+} correspond to three and more surface reflections, thus are noted as Ω_{3+}. This process can be repeated to take into account more surface reflections.

When calculating the average bistatic illumination function or the bidirectional reflectivity, the surface points in Ω_1 and Ω_2 with $\theta_i^{\mathrm{spe}} \in [\theta_i - \Delta\theta_i, \theta_i + \Delta\theta_i]$ are selected. The average bistatic illumination functions $S_B^{1,2}$ equal the ratio of the number of points, N_1 and N_2 selected from Ω_1 and Ω_2, respectively, over the number of the total surface points N_s. The bidirectional reflectivity is obtained from the average reflectivity of each selected path

$$\rho_{1,H,V}^{MC} = \frac{1}{N_s} \sum_{i=1}^{N_1} |r_{H,V}(\chi_{0,i})|^2 g_{0,i},$$

$$\rho_{2,H,V}^{MC} = \frac{1}{N_s} \sum_{i=1}^{N_2} |r_{H,V}(\chi_{0,i})|^2 |r_{H,V}(\chi_{1,i})|^2 g_{0,i}, \qquad \text{(A2)}$$

where $\chi_{0,i}$ and $\chi_{1,i}$ are the local incidence angles at each selected point M_0 and M_1, respectively. Following Eq. (24), $g_{0,i}$ is given by

$$g_0 = 1 - \gamma_{0,i} \, \tan\theta \qquad \text{(A3)}$$

with $\gamma_{0,i}$ being the slope of each selected point M_0.

The hemispherical average illumination function and the hemispherical average reflectivity are calculated in a similar way, but with all points in Ω_1 and Ω_2 being selected, regardless of the direction of $\hat{s}_i^-$. The hemispherical average bistatic illumination function equals the ratio of the number of points N_{Ω_1} and N_{Ω_2} in Ω_1 and Ω_2, respectively, over the number of the total surface points N_s. The hemispherical average reflectivity is the average reflectivity of each path, which is given similarly as Eq. (A2) by replacing N_1 and N_2 with N_{Ω_1} and N_{Ω_2}, respectively.

Finally, the results obtained from each surface are averaged. In this paper, the Monte Carlo results are obtained from 200 surface realizations.

References

1. W. L. Smith, R. O. Knuteson, H. E. Revercomb, W. Feltz, N. R. Nalli, H. B. Howell, W. P. Menzel, O. Brown, J. Brown, P. Minnett, and W. McKeown, "Observations of the infrared radiative properties of the ocean implications for the measurement of sea surface temperature via satellite remote sensing," Bull. Am. Meteorol. Soc. **77**, 41–51 (1996).
2. W. Su, T. P. Charlock, and K. Rutledge, "Observations of reflectance distribution around sunglint from a coastal ocean platform," Appl. Opt. **41**, 7369–7383 (2002).
3. V. Ross, D. Dion, and G. Potvin, "Detailed analytical approach to the Gaussian surface bidirectional reflectance distribution function specular component applied to the sea surface," J. Opt. Soc. Am. A **22**, 2442–2453 (2005).
4. K. Caillault, S. Fauqueux, C. Bourlier, P. Simoneau, and L. Labarre, "Multiresolution optical characteristics of rough sea surface in the infrared," Appl. Opt. **46**, 5471–5481 (2007).
5. V. Ross, D. Dion, and D. St-Germain, "Experimental validation of the modtran 5.3 sea surface radiance model using miramer campaign measurements," Appl. Opt. **51**, 2264–2276 (2012).
6. D. A. Vaitekunas, K. Alexan, O. E. Lawrence, and F. Reid, "Shipir/ntcs: a naval ship infrared signature countermeasure and threat engagement simulator," Proc. SPIE **2744**, 411–424 (1996).
7. C. Bourlier, G. Berginc, and J. Saillard, "Theoretical study on two-dimensional Gaussian rough sea surface emission and reflection in the infrared frequencies with shadowing effect," IEEE Trans. Geosci. Remote Sens. **39**, 379–392 (2001).
8. S. Fauqueux, K. Caillault, P. Simoneau, and L. Labarre, "Multiresolution infrared optical properties for Gaussian sea surfaces: theoretical validation in the one-dimensional case," Appl. Opt. **48**, 5337–5347 (2009).
9. K. Yoshimori, K. Itoh, and Y. Ichioka, "Thermal radiative and reflective characteristics of a wind-roughened water surface," J. Opt. Soc. Am. A **11**, 1886–1893 (1994).
10. P. J. Lynch and R. J. Wagner, "Rough-surface scattering: shadowing, multiple scatter, and energy conservation," J. Math. Phys. **11**, 3032–3042 (1970).
11. C. Bourlier, G. Berginc, and J. Saillard, "Monostatic and bistatic statistical shadowing functions from a one-dimensional stationary randomly rough surface: II. Multiple scattering," Waves Random Media **12**, 175–200 (2002).
12. P. Schott, N. de Beaucoudrey, and C. Bourlier, "Reflectivity of one-dimensional rough surfaces using the ray tracing technique with multiple reflections," in *Geoscience and Remote Sensing Symposium, 2003. IGARSS '03. Proceedings. 2003 IEEE International* (2003), vol. **7**, pp. 4214–4216.
13. J. S. Tyo, D. L. Goldstein, D. B. Chenault, and J. A. Shaw, "Review of passive imaging polarimetry for remote sensing applications," Appl. Opt. **45**, 5453–5469 (2006).
14. H. Li, N. Pinel, and C. Bourlier, "Polarized infrared emissivity of one-dimensional Gaussian sea surfaces with surface reflections," Appl. Opt. **50**, 4611–4621 (2011).
15. R. J. Wagner, "Shadowing of randomly rough surfaces," J. Acoust. Soc. Am. **41**, 138–147 (1967).
16. B. Smith, "Geometrical shadowing of a random rough surface," IEEE Trans. Antennas Propag. **15**, 668–671 (1967).
17. M. Sancer, "Shadow-corrected electromagnetic scattering from a randomly rough surface," IEEE Trans. Antennas Propag. **17**, 577–585 (1969).
18. C. Bourlier, J. Saillard, and G. Berginc, "Intrinsic infrared radiation of the sea surface," Prog. Electromagn. Res. **27**, 185–335 (2000).
19. H. Li, N. Pinel, and C. Bourlier, "A monostatic illumination function with surface reflections from one-dimensional rough surfaces," Waves Random Complex Media **21**, 105–134 (2011).
20. K. Masuda, "Infrared sea surface emissivity including multiple reflection effect for isotropic Gaussian slope distribution model," Remote Sens. Environ. **103**, 488–496 (2006).
21. X. Wu and W. L. Smith, "Emissivity of rough sea surface for 8–13 μm: modeling and verification," Appl. Opt. **36**, 2609–2619 (1997).
22. N. R. Nalli, P. J. Minnett, and P. Delst, "Emissivity and reflection model for calculating unpolarized isotropic water surface-leaving radiance in the infrared. I: theoretical development and calculations," Appl. Opt. **47**, 3701–3721 (2008).
23. P. D. Watts, M. R. Allen, and T. J. Nightingale, "Wind speed effects on sea surface emission and reflection for the along track scanning radiometer," J. Atmos. Ocean. Technol. **13**, 126–141 (1996).
24. C. Cox and W. Munk, "Measurement of the roughness of the sea surface from photographs of the sun's glitter," J. Opt. Soc. Am. **44**, 838–850 (1954).
25. G. M. Hale and M. R. Querry, "Optical constants of water in the 200 nm to 200 μm wavelength region," Appl. Opt. **12**, 555–563 (1973).
26. C. R. Zeisse, C. P. McGrath, K. M. Littfin, and H. G. Hughes, "Infrared radiance of the wind-ruffled sea," J. Opt. Soc. Am. A **16**, 1439–1452 (1999).
27. D. E. Freund, R. I. Joseph, D. J. Donohue, and K. T. Constantikes, "Numerical computations of rough sea surface emissivity using the interaction probability density," J. Opt. Soc. Am. A **14**, 1836–1849 (1997).
28. T. Elfouhaily, B. Chapron, K. Katsaros, and D. Vandemark, "A unified directional spectrum for long and short wind-driven waves," J. Geophys. Res. **102**, 15781–15796 (1997).
29. C. Bourlier, J. Saillard, and G. Berginc, "Effect of correlation between shadowing and shadowed points on the Wagner and Smith monostatic one-dimensional shadowing functions," IEEE Trans. Antennas Propag. **48**, 437–446 (2000).